Chemical Engineering Journal 270 (2015) 196–204

Contents lists available at ScienceDirect

Chemical Engineering Journal

journal homepage: www.elsevier.com/locate/cej

# Mesoporous ZSM5 having both intrinsic acidic and basic sites for cracking and methanation

L.P. Teh [a], S. Triwahyono [a,b,*], A.A. Jalil [c,d], R.R. Mukti [e], M.A.A. Aziz [d], T. Shishido [f]

[a] Department of Chemistry, Faculty of Science, Universiti Teknologi Malaysia, 81310 UTM Johor Bahru, Johor, Malaysia
[b] Ibnu Sina Institute for Fundamental Science Studies, Universiti Teknologi Malaysia, 81310 UTM Johor Bahru, Johor, Malaysia
[c] Institute of Hydrogen Economy, Universiti Teknologi Malaysia, 81310 UTM Johor Bahru, Johor, Malaysia
[d] Department of Chemical Engineering, Faculty of Chemical Engineering, Universiti Teknologi Malaysia, 81310 UTM Johor Bahru, Johor, Malaysia
[e] Division of Inorganic and Physical Chemistry, Faculty of Mathematics and Natural Sciences, Institut Teknologi Bandung, Jl Ganesha No 10, Bandung 40132, Indonesia
[f] Department of Applied Chemistry, Graduate School of Urban Environmental Sciences, Tokyo Metropolitan University, 1-1 Minami-Osawa, Hachioji, Tokyo 192-0397, Japan

## HIGHLIGHTS

- Mesoporous ZSM5 (mZSM5) was prepared by dual templating method.
- High surface area mZSM5 possessed high crystallinity and coffin-shaped morphology.
- mZSM5 possessed intrinsic acidic and basic sites.
- Aging time altered pore distribution, crystallinity and acidic–basic sites of mZSM5.
- mZSM5 is an active catalyst for *n*-heptane cracking and CO methanation.

## GRAPHICAL ABSTRACT

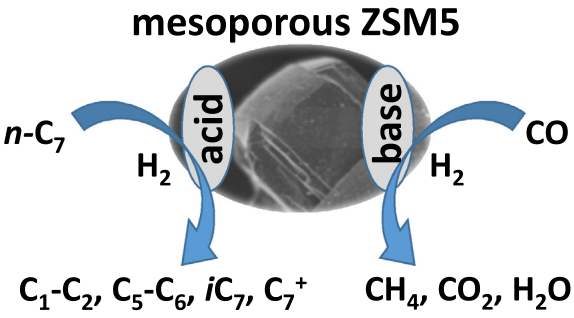


## ARTICLE INFO

*Article history:*
Received 19 November 2014
Received in revised form 20 January 2015
Accepted 22 January 2015
Available online 14 February 2015

*Keywords:*
Mesoporous ZSM5
Dual templating method
Aging times
Micro-mesopores
Intrinsic acidic–basic sites

## ABSTRACT

Mesoporous ZSM5 (mZSM5) was prepared by the dual templating method for *n*-heptane cracking and CO methanation. The properties of mZSM5 were tailored by varying the aging time in the 0.5–3-day range. The physical properties of the catalysts were characterized with XRD, FESEM, nitrogen physisorption and IR. XRD and FESEM analyses indicated that mZSM5s possessed a high crystalline structure with coffin-type morphology. Nitrogen physisorption analysis revealed the presence of both micropores and mesopores in high surface area mZSM5s with inter- and intra-particle porosity. The pyridine and pyrrole adsorbed IR spectroscopy results demonstrated that mZSM5s have both intrinsic acidic and basic sites, which are suitable for acid and/or base catalyzed reactions. The bare mZSM5-0.5D exhibited the highest rate of conversion of *n*-heptane (0.0230 μmol/$m^2$ s) and CO (0.0226 μmol/$m^2$ s) at 573 K and 723 K, respectively. The mZSM5s performed with good stability and no deactivation up to 30 h for *n*-heptane cracking and CO methanation. Co-existence of micro-mesopores and intrinsic acidic–basic sites is vital for acid-catalyzed and base-catalyzed reactions.



## 1. Introduction

Zeolites, are defined as microporous crystalline aluminosilicates and are widely used in a number of industrial processes [1]. Zeolites possess both acidic and basic sites and the dual properties of these sites can play an important role in many catalytic

* Corresponding author at: Department of Chemistry, Faculty of Science, Universiti Teknologi Malaysia, 81310 UTM Johor Bahru, Johor, Malaysia. Tel.: +60 7 5536076; fax: +60 7 5536080.
*E-mail address:* sugeng@utm.my (S. Triwahyono).

http://dx.doi.org/10.1016/j.cej.2015.01.084
1385-8947/

reactions. However, while the acidic properties of zeolites have been extensively explored, their basic properties still remained unclear [2]. Nevertheless, conventional zeolites with relatively small and solely micropores can impose a diffusion limitation problem in many catalytic reactions, which tends to produce coke formation on micropores and lead to faster catalyst deactivation. This has severely limited their catalytic performance. Therefore, coupling the structural features of microporosity and mesoporosity is urgently needed to address this drawback [3,4].

ZSM5 zeolites with MFI-type topology have been widely studied due to the simplicity of mesoporosity introduction and the well-defined nature of the acid sites in conventional zeolite [5]. Although great efforts have been made to obtain mesoporous zeolites, syntheses of mesoporous zeolites are still challengeable to develop periodic mesoporic, tunable, strong acidic/basic, stable and shape-selective microporous zeolites for a wide range of applications. Meso-/microporous zeolites allow facile pore accessibility and fast transportation of bulky molecules and, thus, give good performance in terms of the activity, selectivity and/or stability of zeolite-based catalyzed reactions [6]. A common approach to developing mesoporosity into zeolite crystals is demetallation (desilication or dealumination). However, demetallation suffers from the partial destruction of zeolite structures and the loss of acidic sites.

Tarach et al. [7] found that hierarchical zeolite Beta obtained by a well-adjusted desilication with NaOH and TBAOH could produce mesoporosity and zeolitic microporosity without disturbing the intrinsic acidity of the parent zeolite. This gave better catalytic cracking performances. Keller et al. [8] have discovered hierarchical high-silica USY zeolites through the introduction of intracrystalline mesopores by post-synthetic modification to mitigate diffusion constraints. The importance of mesoporosity and intrinsic zeolitic properties as a function of reactant size was investigated in terms of which of these materials appeared as promising base catalysts and were applicable for a variety of base-catalyzed reactions as well as the upgrading of biofuels. Another strategy is a dual templating method for generating both microporosity and mesoporosity [9,10]. In this approach, surfactant molecules act as a zeolite structure-directing agent and mesoscale template into which they are self-assembled as a supramolecular micelle. Due to the flexible properties of soft templates, they can achieve structural control. Therefore, this method has the highest versatility in terms of altering the mesostructure as compared to other synthesis strategies.

In this study, mesoporous ZSM5 (mZSM5) having intrinsic acidic–basic sites was prepared by the dual templating method for acid-catalyzed and base-catalyzed reactions through *n*-heptane cracking and CO methanation. In the present study, we reported the vital role of aging time to observe the tailoring of material characteristics such as physical, acidic and basic properties which are closely related to the catalytic performance [11,12]. In the present work, *n*-heptane cracking and CO methanation were used as a probe reaction to verify the role of the intrinsic acidic and basic sites of the catalysts, respectively. Catalytic activity of *n*-heptane cracking is demanding on the pore characteristic and acidity in term of concentration and strength of acid sites. However, in this case, acidity is the predominant factor. On the other hand, catalytic performance of CO methanation was strongly affected by both porosity and basicity. The implications of the aging time in the crystallinity, morphology, textural properties, acidity, basicity and catalytic activity of the catalysts were evaluated and discussed. The results showed that high surface area mZSM5s possessed both microporosity and mesoporosity with inter- and intra-particle pores, which significantly determine activity and stability in *n*-heptane cracking and CO methanation.

## 2. Experimental

### 2.1. Catalyst preparation

The mesoporous ZSM5 was prepared by the dual templating method using tetrapropylammonium bromide (TPA-Br) as a micropore-directing agent and benzalkonium chloride as a mesopore-directing agent. The starting parameters were Si/Al = 22.90, $H_2O$/Si = 18.30, TPA-Br/Si = 0.17, benzalkonium chloride/Si = 0.06 and NaOH/Si = 0.15. Firstly, the mixture of benzalkonium chloride, TPA-Br, sodium hydroxide (NaOH) and distilled $H_2O$ was homogeneously mixed at room temperature under vigorous stirring for 5 min. Then, aluminium hydroxide, $Al(OH)_3$ and tetraethyl orthosilicate, $Si(OC_2H_5)_4$ were added and homogeneously mixed at room temperature under vigorous stirring for 3 h. After that, the mixture was transferred into an autoclave and maintained at 423 K to study the effect of aging time. The product was washed, filtered and dried at 383 K for 3 h. The as-synthesized catalyst was calcined at 823 K for 3 h. The prepared catalysts were denoted as mZSM5-0.5D, mZSM5-1D and mZSM5-3D for catalysts with aging times of 0.5, 1 and 3 days, respectively.

### 2.2. Catalyst characterization

The crystalline structure of the catalyst was studied by X-ray diffraction (XRD) and recorded on a powder diffractometer (40 kV, 40 mA) using a Cu K$\alpha$ radiation source in the range of $2\theta$ = 2–50° with a scan rate of 0.1° continuously. The surface morphology of the sample was identified using FESEM-EDX (JEOL JSM-6701F) with an accelerating voltage of 5 kV. The nitrogen physisorption analysis of the catalyst was carried out by using a Beckman Coulter SA3100. Prior to the measurement, approximately 0.05 g of the catalyst were put into a sample tube holder, followed by evacuation at 573 K for 1 h. Then, adsorption of nitrogen was carried out at 77 K. Surface area, pore size distributions and pore volumes were determined from the sorption isotherms using a non-local density functional theory (NLDFT) method. FTIR measurements were performed on an Agilent Cary 640 FTIR spectrometer equipped with a high-temperature stainless steel cell with $CaF_2$ windows. All samples were pretreated at 673 K for 1 h. Pyridine as a basic probe molecule was used to evaluate the acidity of the catalysts. For the pyridine adsorption measurement, the activated catalyst was exposed to 2 Torr of pyridine at 423 K for 15 min, followed by outgassing at 423, 473, 523, 573 and 623 K for 30 min. In the characterization of the basic properties of the catalyst, pyrrole was used as a probe molecule. The activated catalyst was exposed to 4 Torr of pyrrole at room temperature for 5 min, followed by outgassing at 298, 323, 373, 423 and 473 K for 5 min. All spectra were recorded at room temperature.

### 2.3. Catalytic performance

The catalytic cracking of *n*-heptane was carried out in a micro-catalytic pulse reactor at a temperature range of 423–623 K under hydrogen stream. Prior to the reaction, 0.2 g of the catalyst was subjected to oxygen treatment at 673 K for 1 h, followed by $H_2$ reduction at 673 K for 3 h. Then, the reactor was cooled down to a reaction temperature under a hydrogen gas stream. A dose of *n*-heptane (6.8 μmol) was passed over the activated catalyst and the products were trapped at 77 K before being flash-evaporated into an online 6090 N Agilent gas chromatograph equipped with a VZ7 packed column and FID detectors. The intervals between doses were kept constant at 15 min. The rate of *n*-heptane conversion ($r_{n\text{-heptane}}$) was calculated according to Eq. (1):

$$r = k\frac{\sum [C]_i - [C]_{\text{residual } n\text{-heptane}}}{\sum [C]_i} \quad (1)$$

where, $[C]_i$ and $[C]_{\text{residual } n\text{-heptane}}$ represents the molar concentration for a particular product and for residual *n*-heptane. The rate constant ($k$) was determined by the changes of molar concentration of *n*-heptane divided by the surface area and mass of the catalyst per unit time, with the assumption that the retention time for the reactant in the catalyst bed was negligibly small. The selectivity ($S_i$) and yield ($Y_i$) of a particular product was calculated according to Eqs. (2) and (3), respectively:

$$S_i\ (\%) = \frac{[C]_i}{\sum [C]_i - [C]_{\text{residual } n\text{-heptane}}} \times 100 \quad (2)$$

$$Y_i\ (\%) = S_i\frac{r}{k} \quad (3)$$

Carbon monoxide methanation was carried out in a fixed-bed quartz reactor at a temperature range of 423–723 K. Initially, 0.2 g of the catalyst were treated in an oxygen stream for 1 h followed by a hydrogen stream for 3 h at 773 K and cooled down to the desired reaction temperature in a hydrogen stream. When the temperature became stable, a mixture of $H_2$ and CO was fed into the reactor at a specific gas hourly space velocity (GHSV) and $H_2$/CO mass ratio. The composition of the outlet gases was analyzed by an on-line 6090 N Agilent gas chromatograph equipped with a GS-Carbon PLOT column and a TCD detector. CO conversion, $CH_4$ selectivity, $CH_4$ yield and the areal rate were calculated according to the following equations:

$$X_{CO}\ (\%) = \frac{M_{CH_4} + M_{CO_2}}{M_{CO} + M_{CH_4} + M_{CO_2}} \times 100 \quad (4)$$

$$S_{CH_4}(\%) = \frac{M_{CH_4}}{M_{CH_4} + M_{CO_2}} \times 100 \quad (5)$$

$$Y_{CH_4}(\%) = \frac{X_{CO} \times S_{CH_4}}{100} \quad (6)$$

$$\text{Areal rate } (\mu\text{mol CO m}^{-2}\text{ s}^{-1}) = \frac{n_{CO}}{SA \times W_{cat} \times s} \quad (7)$$

where, $X_{CO}$ is the conversion of carbon monoxide (%), $S_{CH_4}$ is the selectivity of $CH_4$ (%) and $Y_{CH_4}$ is the yield of $CH_4$ (%); $M$ is a mole of the CO, $CH_4$ or $CO_2$. The CO conversion rate was expressed in areal rate form. Areal rate is reported as moles of CO converted (μmol CO) divided by the surface area ($m^2\ g^{-1}$), weight of the catalyst (g-cat) and time (s).

Stability testing of *n*-heptane cracking and CO methanation was carried out for 30 h at 573 K and 723 K, respectively. In addition, zeolites, silica and alumina are commonly used as supports for various acid-catalyzed and base-catalyzed reactions [13–19]. Therefore, the catalytic performance of commercial HZSM5, $SiO_2$ and $\gamma$-$Al_2O_3$ was evaluated in *n*-heptane cracking and CO methanation for comparison purposes.

## 3. Results and discussion

### 3.1. Physical properties of the catalysts

The XRD patterns and FESEM images of mZSM5s at different aging times are shown in Fig. 1A and B, respectively. The diffraction peaks in the range of $2\theta$ = 2–50° were identified as characteristic peaks of the MFI type zeolite with high crystallinity [20]. These reflection patterns confirmed the formation of a crystalline MFI type zeolite within the period of 0.5–3 days. Based on the intensity of the peaks, mZSM5-0.5D showed well-developed crystalline

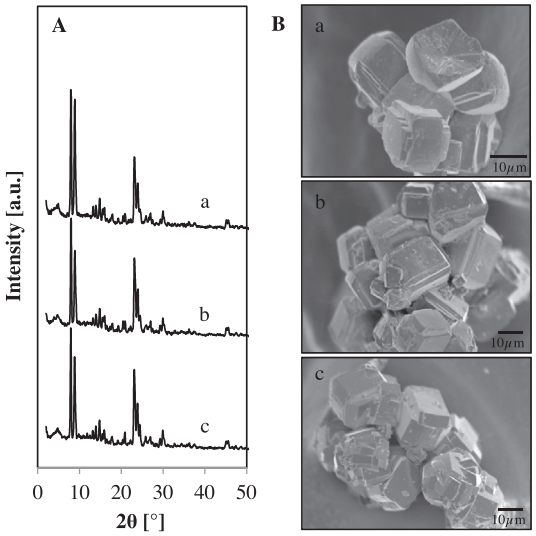


**Fig. 1.** (A) XRD patterns (B) FESEM images of (a) mZSM5-0.5D, (b) mZSM5-1D and (c) mZSM5-3D.

structure followed by mZSM5-1D ≈ mZSM5-3D. This may have been due to the fewer distorted aluminum sites and more ordered framework structure for mZSM5-0.5D [21,22]. In addition, the narrow XRD peaks were in agreement with the large crystals of the ZSM5 zeolite [23].

An FESEM image of mZSM5-0.5D (Fig. 1B-a) showed a well-developed, typical coffin-shaped of ZSM5 with a smooth surface. For mZSM5-1D, coffin-shaped morphology with larger crystal particles was observed due to crystal growth (Fig. 1B-b). For mZSM5-3D, the coffin-like morphology of the ZSM5 zeolite was obtained. However, an aggregation of the particles occurred upon a longer aging period of mZSM5 (Fig. 1B-c) [23]. The results of XRD and FESEM analyses confirmed the successful preparation of mZSM5s.

Fig. 2 illustrates the $N_2$ adsorption–desorption isotherm and pore size distribution of different aging times of mZSM5. All mZSM5s demonstrated a type IV isotherm with a type H1 hysteresis loop (IUPAC classification), which is analogous to that observed in the MCM-41 support and which significantly contrasts with that of conventional ZSM5 [24]. The type H1 hysteresis loop is characteristic of capillary condensation in an open-ended cylindrical channel with a uniform size and shape. A high adsorption volume of nitrogen indicates the presence of mesopores in mZSM5s [25,26]. All mZSM5s showed a sharp uptake at low relative pressure, which is indicative of micropores in zeolite ZSM5. Additionally, these mZSM5s showed two steps of capillary condensation with the first step at P/Po = 0.2–0.4 attributed to mesopores inside the mZSM5 (intraparticles). Secondly, the higher relative pressure of P/Po = 0.9–1.0 is attributed to nitrogen condensation that occurs in interparticle pores [27,28]. Furthermore, a significant up-step at the relative pressure of $P/P_O$ = 0.2–0.4 was due to the capillary condensation of nitrogen in the channels which reflects a narrow pore size distribution. Although the typical adsorption steps were observed for all mZSM5s, mZSM5-0.5D showed the highest nitrogen adsorption compared to the others. This was due to the larger pore volume and pore size distribution. In the present study, we analyzed by applying non-local density functional theory (NLDFT) method. The NLDFT method is applicable to micro-mesoporous materials [29]. It allows calculating the specific cumulative surface area (i.e., specific surface area as a function of pore size) over the complete range of micro- and mesopores. Based on previous literatures, the surface area of conventional ZSM5 is in the range of 400–500 $m^2\ g^{-1}$ [30–32]. All mZSM5s exhibited a significant pore

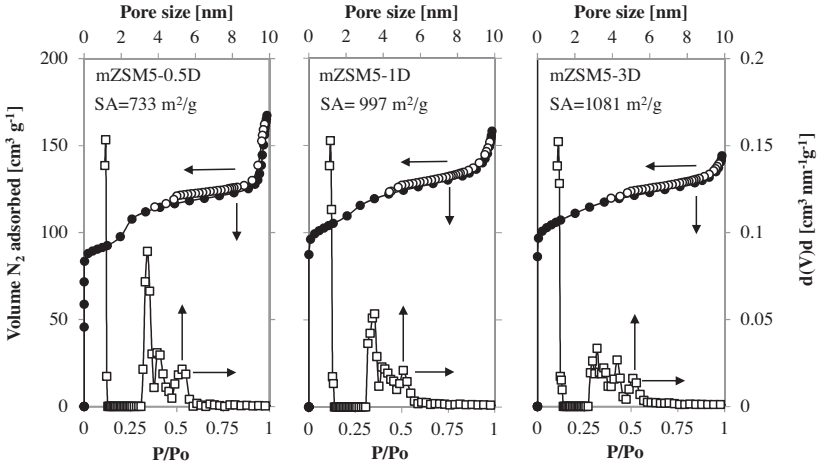


**Fig. 2.** $N_2$ adsorption–desorption isotherm and NLDFT pore size distribution of different aging times of mZSM5.

size distribution in the narrow range of 3–6 nm. The peak observed around 3–6 nm does not reflect the exact porous properties of the material but is determined primarily by the nature of the adsorption. For surface area analysis, mZSM5s had a high surface area with 733, 997 and 1081 $m^2\ g^{-1}$ for mZSM5-0.5D, mZSM5-1D and mZSM5-3D, respectively (Table 1). The surface area of mZSM5s was higher than conventional ZSM5. This suggests the co-existence of micropores and mesopores [30]. Furthermore, the total pore volume for mZSM5-0.5D, mZSM5-1D and mZSM5-3D was 0.2480, 0.2417 and 0.2276 $cm^3\ g^{-1}$, respectively (Table 1). A high volume of pore distribution was created upon aging at 0.5 days and decreased after a longer aging period. The larger pore volume of mZSM5-0.5D was related to higher nitrogen adsorption at P/Po = 0.9–1.0 due to the small particle size of mZSM5-0.5D. The specific surface area increased with increasing aging time, as well as the total pore volume decreased. This may be due to the reduction of the intraparticle pores observed in P/Po = 0.2–0.4 and transformation of the small size micropores to the bigger pore size as shown in Fig. 2. mZSM5-0.5D had a larger total pore volume and mesopore volume with a lower surface area and micropore volume. However, mZSM5-0.5D possessed a larger mesopore surface area compared to the others. These $N_2$ adsorption–desorption results further confirmed the formation of mesoporous ZSM5s.

### 3.2. Intrinsic acidity and basicity of the catalysts

The nature of acidic and basic sites of the mZSM5 catalysts were determined by FTIR of adsorbed pyridine and pyrrole as shown in the IR spectra (Figs. 3–6). Brönsted acid sites are ascribed to bridging OH groups between tetrahedrally coordinated Al and Si atoms while Lewis acid sites have been associated with the presence of trigonally coordinated aluminum and extra framework aluminum (EFAL) [33]. Fig. 3 shows the IR spectra of the pyridine adsorbed on activated mZSM5s at (a) 423 K and followed by outgassing at different temperatures (spectra b to f). The bands at 1546 and 1442 $cm^{-1}$ are ascribed to pyridinium ions (pyridine adsorbed on Brönsted acid sites) and pyridine adsorbed on Lewis acid sites, respectively [34]. Intrinsic zeolites basicity is of the Lewis type and associated with the lattice oxygen atoms bearing a negative charge. It increases as the framework Al content increases and enhances as the electropositive character of the nonframework compensating cations increases. Pyrrole was used as probe molecules for basic sites of the ZSM5 zeolite because NH bond polarization increases with intrinsic zeolite basicity [35]. Fig. 4 shows the IR spectra of pyrrole adsorbed on activated mZSM5s in the region of 4000–2800 $cm^{-1}$. The spectra were recorded after the adsorption of pyrrole at (a) room temperature, followed by outgassing

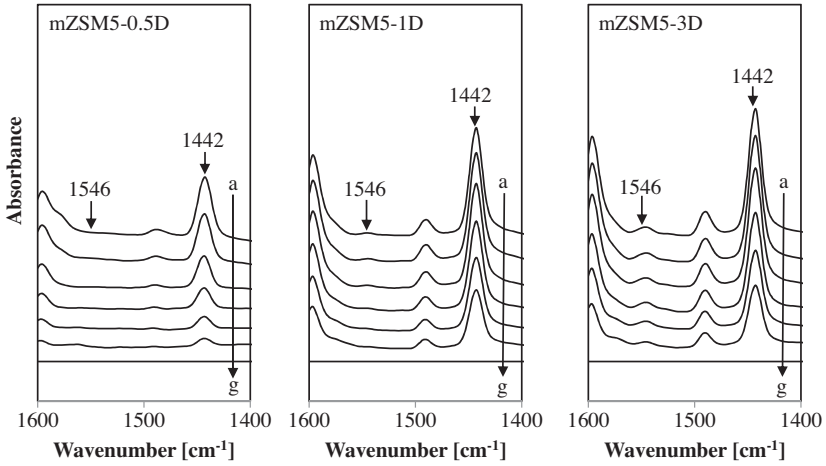


**Fig. 3.** IR spectra of pyridine adsorbed on activated mZSM5s at (a) 423 K followed by outgassing at (b) 423 K, (c) 473 K, (d) 523 K, (e) 573 K and (f) 623 K. (g) Before exposure to pyridine.

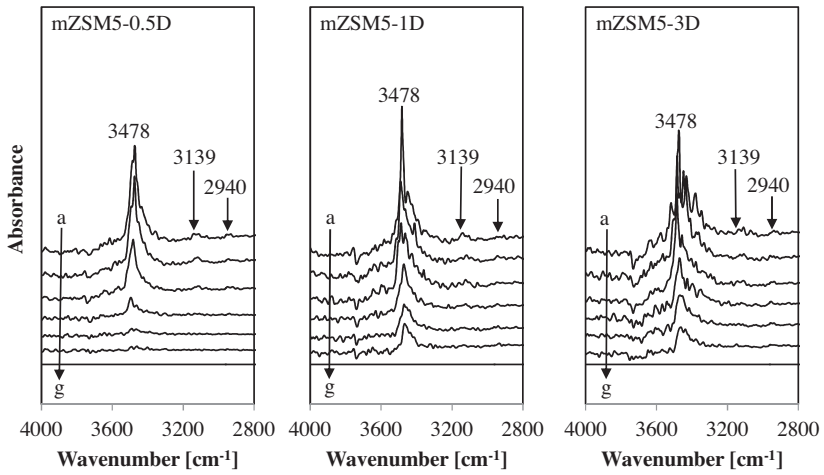


**Fig. 4.** IR spectra of pyrrole adsorbed on activated mZSM5s at (a) 298 K followed by outgassing at (b) 298 K, (c) 323 K, (d) 373 K, (e) 423 K and (f) 473 K. (g) Before exposure to pyrrole.

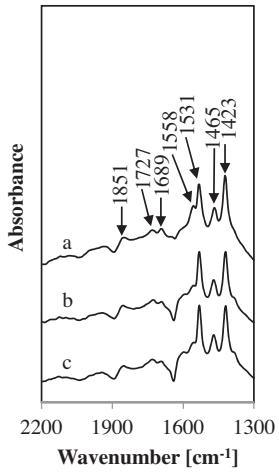


**Fig. 5.** IR spectra of pyrrole adsorbed on activated catalysts after outgassing at 298 K in the range of 2200–1300 $cm^{-1}$ for (a) mZSM5-0.5D, (b) mZSM5-1D and (c) mZSM5-3D.

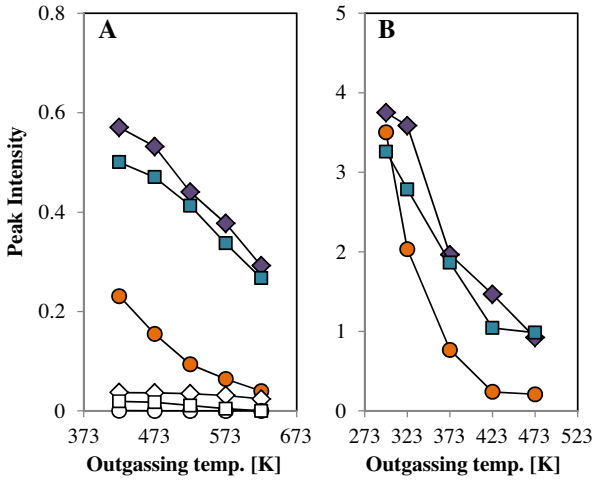


**Fig. 6.** (A) Variations of the absorbances of the IR bands at 1546 $cm^{-1}$ (open symbol) and 1442 $cm^{-1}$ (filled symbol) as a function of outgassing temperature after pyridine adsorption for mZSM5-0.5D (○, ●), mZSM5-1D (□, ■) and mZSM5-3D (◇, ◆). (B) Variations of the absorbance of the IR bands at 3478 $cm^{-1}$ as a function of outgassing temperature after pyrrole adsorption for mZSM5-0.5D (●), mZSM5-1D (■) and mZSM5-3D (◆). Sample was activated at 673 K.

at different temperatures (spectra b–f). For all catalysts, the main broad band situated at about 3700–3270 $cm^{-1}$ can be assigned to N–H stretching vibrations of chemisorbed pyrrole ($C_4H_4NH$) interacting with the framework oxygen atoms by hydrogen bonding ($C_4H_4NH$–$O_{zeol}$) and interacting via aromatic system with the non-framework cations. Both interactions happen simultaneously and influence each other [36]. The band at 3478 $cm^{-1}$ is attributed to the perturbed N–H stretch of pyrrole molecules interacting with the surface of the basic sites [37]. The high intensity indicates a high concentration of basic sites possessed by the catalyst. Furthermore, the band at 3139 $cm^{-1}$ is attributed to the pyrrole in a liquid phase with medium strength while the band at 2940 $cm^{-1}$ is assigned to a fundamental aliphatic ν(CH) vibration [38]. As shown in Fig. 5, the complexity of the IR spectra in the region of 2200–1300 $cm^{-1}$ shows a series of bands at 1851, 1727, 1689, 1558, 1531, 1465 and 1423 $cm^{-1}$. Among these bands, two intense bands at 1531 and 1423 $cm^{-1}$ are observed, which are attributed to the formation of non-dissociated pyrrole hydrogen bound to basic $O^{2-}$ [37].

Fig. 6 A shows the variations of the IR bands at 1546 and 1442 $cm^{-1}$ as a function of the outgassing temperature from 423–623 K after pyridine adsorption for the mZSM5s catalyst. The amount of coordinated pyridine on the acidic sites was calculated from the intensity of the bands at 1546 and 1442 $cm^{-1}$ for which the integrated molar extinction coefficients were 1.67 cm μmol$^{-1}$ for the Brönsted and 2.22 cm μmol$^{-1}$ for the Lewis acid sites [39]. At 423 K, the amount of pyridine adsorbed on the Brönsted acid sites is 0.01, 0.90 and 1.76 μmol $g^{-1}$, and the amount of pyridine adsorbed on Lewis acid sites is 14.48, 31.36 and 35.75 μmol $g^{-1}$ for mZSM5-0.5D, mZSM5-1D and mZSM5-3D, respectively (Table 1). The band at 1546 $cm^{-1}$ was slightly decreased while the band at 1442 $cm^{-1}$ was markedly decreased with an outgassing temperature from 423 to 623 K. These results indicated the presence of strong Lewis acid sites for all mZSM5s. In addition, there is a considerable number of weak Brönsted and Lewis acid sites from which they were desorbed after outgassing at temperatures from 423 to 623 K. Fig. 6 B shows the variations of IR bands at 3478 $cm^{-1}$ as a function of an outgassing temperature from 298–473 K after pyrrole adsorption for mZSM5 catalysts. The number of basic sites of the catalysts decreased following the order mZSM5-3D > mZSM5-1D > mZSM5-0.5D. It is

noteworthy that mZSM5-0.5D showed fewer available sites for the adsorption of pyrrole than did the other mZSM5. This result showed that fewer pyrrole adsorption sites led to a decrease in CO adsorption on mZSM5-0.5D. It also indicated that higher pyrrole adsorption sites on mZSM5-1D and mZSM5-3D may be due to the presence of higher basic structural defects [38].

### 3.3. Catalytic performance

Fig. 7A and C show *n*-heptane cracking (at 373–673 K) and CO methanation (at 400–800 K) as a function of reaction temperatures. It is noteworthy that unmodified mZSM5 is capable of *n*-heptane cracking and CO methanation. The rate conversion of *n*-heptane increased gradually from 423–573 K and slightly declined when the temperature reached 623 K. The percentage decrease of the rate conversion of *n*-heptane for mZSM5-0.5D, mZSM5-1D and mZSM5-3D is 1.41%, 0.85% and 0.71%, respectively. The slight monotonic decrease in the rate conversion of *n*-heptane cracking may be due to coke formation, which blocks the accessibility of the reactants to the active sites of the mZSM5s [26,40,41]. But, these results did not significantly affect catalytic performance. In the conversion of CO over mZSM5s, the rate of conversion increased slightly as the reaction temperature increased from 423–723 K and markedly increased at 723 K. mZSM5-0.5D showed the highest rate of conversion of *n*-heptane (0.0230 μmol/m$^2$ s) and CO (0.0226 μmol/m$^2$ s) at 573 K and 723 K, respectively. The stability test of mZSM5s for *n*-heptane cracking at 573 K and CO methanation at 723 K was conducted for 30 h where the rate of conversion of reactants was plotted as a function of pulse number and time on stream, respectively. As shown in Fig. 7B and D, when pulse number/time on stream increases, the rate conversion of both reactions for mZSM5s shows no obvious decrease. The mZSM5s prepared did not show any sign of deactivation for *n*-heptane cracking and CO methanation reaction up to 30 h. Thus, mZSM5s presented good stability under reaction conditions. Tanggarnjanavalukul et al. [15] investigated the pore characteristics of silica supports on prolonging the lifetime of catalysts from coke deposition in methane cracking reaction. From the study, the highest catalytic activity and longest stability was obtained on Ni loaded on bimodal porous silica-5 (Ni/BPS-5) at 773 K. This is due to the existence of a mesopore–macropore structure and a larger pore size on Ni/BPS-5, leading to a higher effective diffusion coefficient.

Fig. 8 shows the product distribution of different aging times of mZSM5 for *n*-heptane cracking and CO methanation at 573 and 723 K, respectively. For *n*-heptane cracking, the outlet was composed of low cracking products ($C_1$–$C_2$), $C_5$–$C_6$, isoheptane and higher hydrocarbons with $C_1$–$C_2$ showed a main contribution with selectivity of >80%. The production of methane is obtained from syngas (a mixture of CO and $H_2$) via the CO methanation process. Besides, the water–gas shift (WGS) reaction and reverse reaction may happen as a side reaction [42–45]. The catalytic performance results showed that conversion of CO was markedly increased at 723 K, possibly due to the increase in the methanation activity accompanied by the water–gas shift (WGS) reaction [46]. In the CO methanation over mZSM5s, the products were composed of methane and carbon dioxide; only mild $H_2O$ was observed in our experiments. So, it is plausible that the CO methanation process over mZSM5s occurred with both water–gas shift and reverse reaction. mZSM5-0.5D gave the highest selectivity to methane (71.4%) followed by mZSM5-3D (70.7%) and mZSM5-1D (68.7%). In this report, the absence of metal active sites gave the actual elucidation of the effect of intrinsic acidic–basic sites towards *n*-heptane cracking and CO methanation. mZSM5-0.5D showed the highest activity and selectivity for both *n*-heptane cracking and CO methanation due to the presence of a high surface area, mesoporosity and intrinsic acidic–basic sites. The detailed results are listed in Table 2.

Fig. 9 shows the product yield of *n*-heptane cracking at 573 K and CO methanation at 723 K for mZSM5s, HZSM5, $SiO_2$ and γ-$Al_2O_3$. For the results, mZSM5–5s produced a comparable yield of $C_1$–$C_2$ in *n*-heptane cracking and showed superior performance in CO methanation as compared to other catalysts. Notably, higher

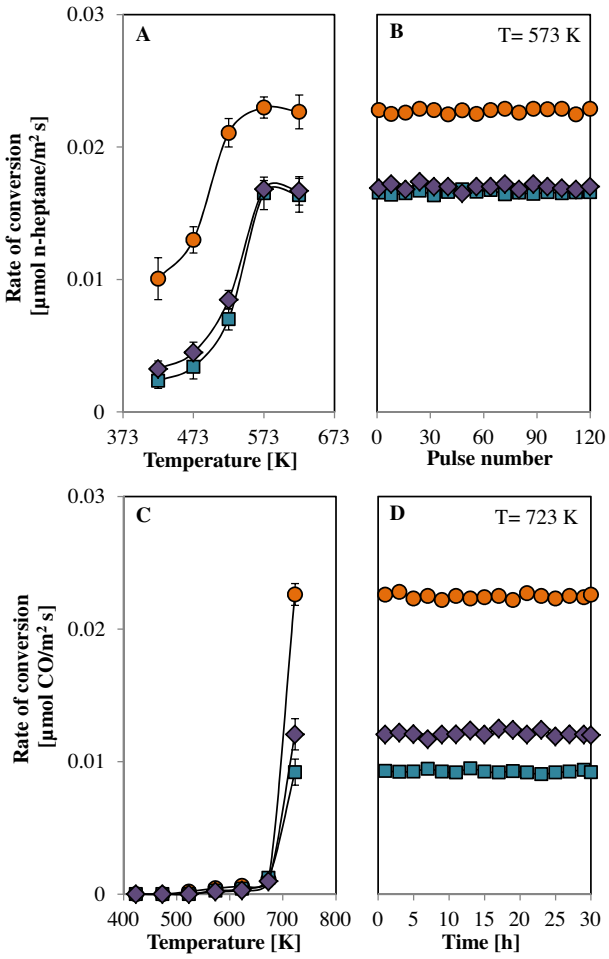


**Fig. 7.** Rate of conversion of (A) *n*-heptane, (C) CO as a function of the reaction temperature and stability testing of (B) *n*-heptane cracking at 573 K, (D) CO methanation at 723 K as a function of pulse number and time-on-stream, respectively, over mZSM5-0.5D (●), mZSM5-1D (■) and mZSM5-3D (◆).

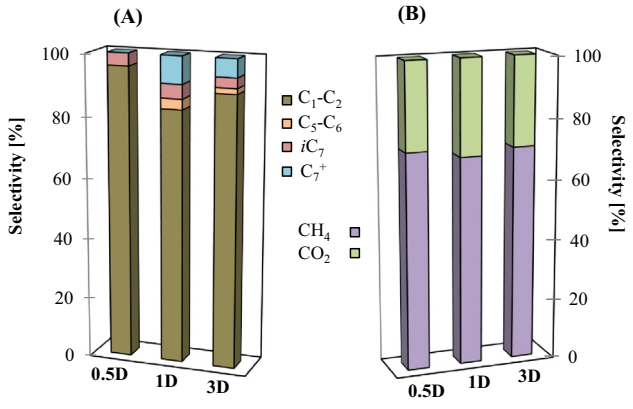


**Fig. 8.** Product distribution of mZSM5-0.5D, mZSM5-1D and mZSM5-3D in (A) *n*-heptane cracking at 573 K and (B) CO methanation at 723 K.

**Table 1**
Textural properties and acidity of different aging times of mZSM5.

| Catalysts | Surface area ($m^2\ g^{-1}$) | Total pore volume ($cm^3\ g^{-1}$) | Brönsted acid site[a,b] ($\mu mol\ g^{-1}$) | Lewis acid site[a,b] ($\mu mol\ g^{-1}$) |
|---|---|---|---|---|
| mZM5-0.5D | 733 | 0.2480 | 0.01 | 14.48 |
| mZM5-1D | 997 | 0.2417 | 0.90 | 31.36 |
| mZM5-3D | 1081 | 0.2276 | 1.76 | 35.75 |

[a] Amount of pyridine adsorbed at 423 K.
[b] The amount of Brønsted and Lewis acid sites was calculated using the integrated molar extinction coefficients for which $\varepsilon_{1546} = 1.67\ cm\ \mu mol^{-1}$ for the Brönsted and $\varepsilon_{1442} = 2.22\ cm\ \mu mol^{-1}$ for the Lewis acid sites.

isomer products were observed for mZSM5s as compared to $SiO_2$ and $\gamma$-$Al_2O_3$, but this was lower than HZSM5. This may due to the presence of a higher surface area and mesoporosity in mZSM5s, which contributed to the accessibility of higher active sites. In addition, our research group has reported that the amount of strong Lewis acid sites significantly influenced the formation of protonic acid sites originating from molecular hydrogen, which is required in the isomerization reaction [47]. Moreover, mZSM5s may demonstrate a different reaction mechanism in contrast with HZSM5, $SiO_2$ and $\gamma$-$Al_2O_3$. For mZSM5s, the cracking process may proceeded via a hydrogenolysis process while for HZSM5, $SiO_2$ and $\gamma$-$Al_2O_3$, a dimerization-cracking reaction route occurs. The presence of $C_1$ and $C_2$ products evidenced for the occurrence of hydrogenolysis process which the carbon–carbon single bond is cleaved or undergoes "lysis" by hydrogen [48,49] (Table 2).

Catalytic cracking results were verified with respect to acidity and the textural properties of the catalysts. The influence of intrinsic acidity on the catalytic cracking of *n*-heptane is more demanding on the concentration and the strength of acid sites due to the linear chain *n*-heptane, which is able to diffuse through the complete system of channels. Milina et al. [5] reported that post-synthetic modification of hierarchical ZSM5 zeolites greatly improves catalytic performance, which is strongly influenced by both porosity and acidic properties. In addition, Chen et al. [50] also reported a correlation between pore structure and acidic properties and the improvement of hydrocarbon conversion. They stated that proper pore structure and suitable (Brönsted + Lewis) acid sites are needed for activity enhancement in *n*-heptane cracking. Liu et al. [51] studied the hydroconversion of *n*-heptane over Pt/Al-MCM-41 samples with various pore sizes. They reported that the acidity and the pore structure of the support materials affecting catalytic performance and final product distribution, assuming the hydrogenating/dehydrogenating function, is not the limiting step.

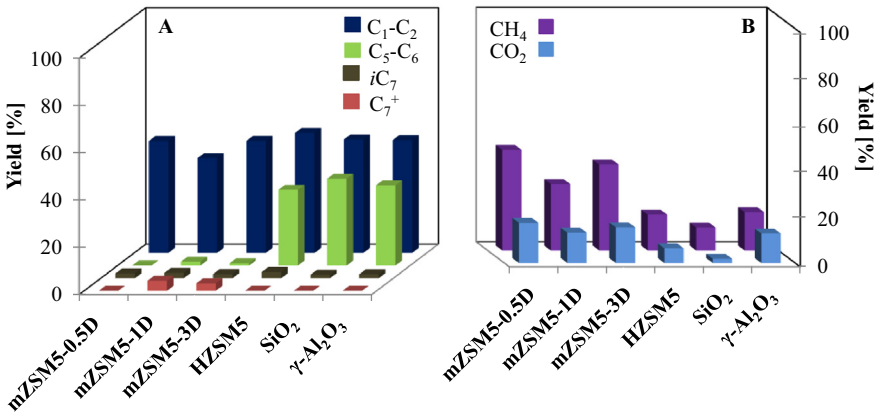


**Fig. 9.** Product yield of (A) *n*-heptane cracking at 573 K and (B) CO methanation at 723 K for various catalysts.

**Table 2**
Product distribution for *n*-heptane cracking and CO methanation over mZSM5-0.5D, mZSM5-1D and mZSM5-3D.

| | mZSM5-0.5D | | | | | mZSM5-1D | | | | | mZSM5-3D | | | | |
|---|---|---|---|---|---|---|---|---|---|---|---|---|---|---|---|
| *n-Heptane cracking* | | | | | | | | | | | | | | | |
| React. Temp. (K) | 423 | 473 | 523 | 573 | 623 | 423 | 473 | 523 | 573 | 623 | 423 | 473 | 523 | 573 | 623 |
| Rate of conversion [$\mu mol\ n\text{-}C_7/m^2\ s$] | 0.0101 | 0.013 | 0.0211 | 0.023 | 0.0228 | 0.0023 | 0.0034 | 0.007 | 0.0165 | 0.0164 | 0.0032 | 0.0045 | 0.0085 | 0.0168 | 0.0167 |
| Selectivity (%) | | | | | | | | | | | | | | | |
| $C_1$–$C_2$ | 98.8 | 98.4 | 86.0 | 95.9 | 95.2 | 0 | 97.3 | 84.9 | 83.1 | 98.7 | 95.7 | 97.7 | 97.0 | 89.0 | 96.7 |
| $C_5$–$C_6$ | 0 | 0 | 0 | 0 | 1.2 | 0 | 0 | 2.0 | 3.4 | 0.5 | 0 | 0 | 1.4 | 1.8 | 0.4 |
| $iC_7$ | 1.2 | 1.6 | 4.4 | 4.1 | 3.6 | 14.2 | 2.7 | 1.8 | 4.6 | 0.8 | 4.3 | 2.3 | 1.6 | 3.3 | 2.9 |
| $C_7^+$ | 0 | 0 | 9.6 | 0 | 0 | 85.8 | 0 | 11.3 | 8.9 | 0 | 0 | 0 | 0 | 5.9 | 0 |
| Yield of cracking (%) | 21.3 | 27.5 | 43.3 | 47.3 | 46.9 | 5.9 | 9.6 | 20.0 | 46.0 | 47.4 | 9.8 | 13.8 | 26.4 | 51.5 | 51.3 |
| *CO methanation* | | | | | | | | | | | | | | | |
| React. Temp. (K) | 523 | 573 | 623 | 673 | 723 | 523 | 573 | 623 | 673 | 723 | 523 | 573 | 623 | 673 | 723 |
| Rate of conversion [$\mu mol\ CO/m^2\ s$] | 0.0002 | 0.0004 | 0.0006 | 0.0011 | 0.0226 | 0 | 0.0003 | 0.0004 | 0.0012 | 0.0092 | 0 | 0.0002 | 0.0003 | 0.001 | 0.0121 |
| Selectivity (%) | | | | | | | | | | | | | | | |
| $CH_4$ | 100 | 100 | 100 | 100 | 71.4 | 0 | 100 | 100 | 100 | 68.7 | 0 | 100 | 100 | 100 | 70.7 |
| $CO_2$ | 0 | 0 | 0 | 0 | 28.6 | 0 | 0 | 0 | 0 | 31.3 | 0 | 0 | 0 | 0 | 29.3 |
| Yield of $CH_4$ (%) | 0.9 | 2.0 | 2.9 | 5.1 | 42.9 | 0 | 1.7 | 2.5 | 7.6 | 28.4 | 0 | 1.3 | 2.0 | 6.5 | 36.7 |

However, this assumption is only applicable for mesoporous materials with weak acidity. Besides, they also stated that materials with larger pore sizes can be used to solve the diffusion problems, which are commonly encountered in conventional microporous zeolites, as a dramatic effect of pore size on catalytic performance was observed. Similarly, mZSM5s may resemble the same phenomenon. Methanation of carbon oxide (CO and/or $CO_2$) is a basic reaction and is highly exothermic. Aziz et al. [52] reported that a high concentration of basic sites and a presence of defect sites or oxygen vacancies contributing to the high activity of $CO_2$ methanation in Ni-promoted mesostructured silica nanoparticles (Ni/MSN). Additionally, Pan et al. [53] proposed that medium basic sites are required to enhance $CO_2$ methanation activity over ceria-zirconia oxides. Moreover, Razzaq et al. [54] studied the co-methanation of carbon oxides (CO and $CO_2$) with a highly active and stable $Co_4N/\gamma$-$Al_2O_3$ catalyst. The $20Co_4N/\gamma$-$Al_2O_3$ catalyst showed excellent catalytic performance with $Co_4N$ as a superior active phase for CO and $CO_2$ conversion and higher surface basicity with incorporation of "N". Besides, introducing mesoporosity into conventional zeolite may result in enhanced acid site accessibility and mass transport to or from an active site. He et al. [6] studied the catalytic consequences of micropore topology, mesoporosity and acidity on the hydrolysis of sucrose over zeolite catalysts. It has been shown that meso-/microporous MWW and MFI zeolites have higher activity compared to their microporous analogues. This may be due to fewer diffusion limitations and abundant acid site accessibility. In addition, Zhang et al. reported the good performance of mesoporous molecular sieve (MSU-1) shell to overcome the transport resistance problem of microporous Sil-1 zeolite shell for methane steam reforming in a direct internal reforming molten carbonate fuel cell [55]. Besides, Kiatphuengporn et al. stated that pore characteristics of the supports will strongly affected the catalytic performance of $CO_2$ hydrogenation [56].

## 4. Conclusion

We successfully prepared high surface area mesoporous ZSM5 by the dual templating method for *n*-heptane cracking and CO methanation. Mesoporous ZSM5 was tailored by varying the aging time in the 0.5–3-day range. Small variations in aging times have large impact on the zeolite properties. From this study, mZSM5-0.5D appeared to be the best catalyst. The catalytic activity of *n*-heptane cracking and CO methanation followed the order mZSM5-0.5D > mZSM5-3D > mZSM5-1D at 573 K and 723 K, respectively. Additionally, bare mZSM5s showed remarkably good stability. The catalytic activity of mZSM5s was closely related to the physical properties, intrinsic acidity and basicity of the catalysts. The high surface area mZSM5s possessed high crystallinity, coffin-type morphology and micro-mesoporosity with the presence of inter and intra-particle pores, and, importantly, dual intrinsic acidic–basic sites, which are potential candidates to be widely used in acid-catalyzed and base-catalyzed reactions.

## Acknowledgments

This work was supported by the Universiti Teknologi Malaysia through Research University Grant No. 10J64 and MyPhd Scholarship (Teh Lee Peng) from the Ministry of Higher Education, Malaysia.

## References

[1] J. Coronas, Present and future synthesis challenges for zeolites, Chem. Eng. J. 156 (2010) 236–242.
[2] D. Murphy, P. Massiani, R. Franck, D. Barthomeuf, Basic site heterogeneity and location in alkali cation exchanged EMT zeolite. An IR study using adsorbed pyrrole, J. Phys. Chem. 100 (1996) 6731–6738.
[3] L.-H. Chen, X.-Y. Li, J.C. Rooke, Y.-H. Zhang, X.-Y. Yang, Y. Tang, F.-S. Xiao, B.-L. Su, Hierarchically structured zeolites: synthesis, mass transport properties and applications, J. Mater. Chem. 22 (2012) 17381–17403.
[4] J. Yang, S. Yu, H. Hu, Y. Zhang, J. Lu, J. Wang, D. Yin, Synthesis of ZSM-5 hierarchical microsphere-like particle by two stage varying temperature crystallization without secondary template, Chem. Eng. J. (2011) 1083–1089.
[5] M. Milina, S. Mitchell, N.-L. Michels, J. Kenvin, J. Pérez-Ramírez, Interdependence between porosity, acidity, and catalytic performance in hierarchical ZSM-5 zeolites prepared by post-synthetic modification, J. Catal. 308 (2013) 398–407.
[6] Y. He, T.C. Hoff, L. Emdadi, Y. Wu, J. Bouraimaa, D. Liu, Catalytic consequences of micropore topology, mesoporosity, and acidity on the hydrolysis of sucrose over zeolite catalysts, Catal. Sci. Technol. 4 (2014) 3064–3073.
[7] K. Tarach, K. Góra-Marek, J. Tekla, K. Brylewska, J. Datka, K. Mlekodaj, W. Makowski, M.C. Igualada López, J. Martínez Triguero, F. Rey, Catalytic cracking performance of alkaline-treated zeolite Beta in the terms of acid sites properties and their accessibility, J. Catal. 312 (2014) 46–57.
[8] T.C. Keller, S. Isabettini, D. Verboekend, E.G. Rodrigues, J. Pérez-Ramírez, Hierarchical high-silica zeolites as superior base catalysts, Chem. Sci. 5 (2014) 677–684.
[9] H. Jin, M.B. Ansari, S.-E. Park, Mesoporous MFI zeolites by microwave induced assembly between sulfonic acid functionalized MFI zeolite nanoparticles and alkyltrimethylammonium cationic surfactants, Chem. Commun. 47 (2011) 7482–7484.
[10] D.P. Serrano, J.M. Escola, P. Pizarro, Synthesis strategies in the search for hierarchical zeolites, Chem. Soc. Rev. 42 (2013) 4004–4035.
[11] C.J. Van Oers, K. Góra-Marek, K. Sadowska, M. Mertens, V. Meynen, J. Datka, P. Cool, In situ IR spectroscopic study to reveal the impact of the synthesis conditions of zeolite b nanoparticles on the acidic properties of the resulting zeolite, Chem. Eng. J. 237 (2014) 372–379.
[12] B. Liu, L. Zheng, Z. Zhu, K. Zhang, H. Xi, Y. Qian, Effect of synthesis conditions on the structural and catalytic properties of hierarchically structured ZSM-5 zeolites, RSC Adv. 4 (2014) 13831–13838.
[13] K. Kubo, H. Iida, S. Namba, A. Igarashi, Comparison of steaming stability of Cu-ZSM-5 with those ofAg-ZSM-5, P/H-ZSM-5, and H-ZSM-5 zeolites as naphtha cracking catalysts to produce light olefin at high temperatures, Appl. Catal., A: Gen. 489 (2015) 272–279.
[14] R. Javaid, K. Urata, S. Furukawa, T. Komatsu, Factors affecting coke formation on H-ZSM-5 in naphtha cracking, Appl. Catal., A: Gen. 491 (2015) 100–105.
[15] C. Tanggarnjanavalukul, W. Donphai, T. Witoon, M. Chareonpanich, J. Limtrakul, Deactivation of nickel catalysts in methane cracking reaction: effect of bimodal meso-macropore structure of silica support, Chem. Eng. J. 262 (2015) 364–371.
[16] X. Hu, C. Li, C. Yang, Studies on lattice oxygen utilization during catalytic conversion of n-heptane activated by $V_2O_5/Al_2O_3$, Chem. Eng. J. 263 (2015) 113–118.
[17] I. Graca, L.V. González, M.C. Bacariza, A. Fernandes, C. Henriques, J.M. Lopes, M.F. Ribeiro, $CO_2$ hydrogenation into $CH_4$ on NiHNaUSY zeolites, Appl. Catal., B: Environ. 147 (2014) 101–110.
[18] C. Yuan, N. Yao, X. Wang, J. Wang, D. Lv, X. Li, The $SiO_2$ supported bimetallic Ni–Ru particles: a good sulfur-tolerant catalyst for methanation reaction, Chem. Eng. J. 260 (2015) 1–10.
[19] J. Li, L. Zhou, P. Li, Q. Zhu, J. Gao, F. Gu, F. Su, Enhanced fluidized bed methanation over a $Ni/Al_2O_3$ catalyst for production of synthetic natural gas, Chem. Eng. J. 219 (2013) 183–189.
[20] Z. Bohström, H. Härelind, B. Gevert, S.-I. Anderssona, K. Holmberg, Comparison of microporous/mesoporous and microporous HZSM-5 as catalysts for Friedel–Crafts alkylation of toluene with ethene, RSC Adv. 4 (2014) 28786–28793.
[21] D. Fodor, L. Pacosová, F. Krumeichb, J.A. van Bokhoven, Facile synthesis of nano-sized hollow single crystal zeolites under mild conditions, Chem. Commun. 50 (2014) 76–78.
[22] H.D. Setiabudi, A.A. Jalil, S. Triwahyono, N.H.N. Kamarudin, R.R. Mukti, IR study of iridium bonded to perturbed silanol groups of Pt-HZSM5 for n-pentane isomerization, Appl. Catal., A: Gen. 417–418 (2012) 190–199.
[23] C. Liu, W. Gu, D. Kong, H. Guo, The significant effects of the alkali-metal cations on ZSM-5 zeolite synthesis: from mechanism to morphology, Microporous Mesoporous Mater. 183 (2014) 30–36.
[24] S. Kelkar, C.M. Saffron, Z. Li, S.-S. Kim, T.J. Pinnavaia, D.J. Millerb, R. Kriegele, Aromatics from biomass pyrolysis vapour using a bifunctional mesoporous catalyst, Green Chem. 16 (2014) 803–812.
[25] B. Puértolas, L. García-Andújar, T. García, M.V. Navarro, S. Mitchell, J. Pérez-Ramírez, Bifunctional Cu/H-ZSM-5 zeolite with hierarchical porosityfor hydrocarbon abatement under cold-start conditions, Appl. Catal., B: Environ. 154–155 (2014) 161–170.
[26] Y. Wu, L. Emdadi, Z. Wang, W. Fan, D. Liu, Textural and catalytic properties of Mo loaded hierarchical meso-/microporous lamellar MFI and MWW zeolites for direct methane conversion, Appl. Catal., A: Gen. 470 (2014) 344–354.
[27] M. Kubů, M. Opanasenko, M. Shamzy, Modification of textural and acidic properties of -SVR zeoliteby desilication, Catal. Today 227 (2014) 26–32.
[28] X. Wang, X. Zhang, Y. Wang, H. Liu, J. Qiu, J. Wang, W. Han, K.L. Yeung, Investigating the role of zeolite nanocrystal seeds in the synthesis of mesoporous catalysts with zeolite wall structure, Chem. Mater. 23 (2011) 4469–4479.
[29] J. Landers, G.Y. Gor, A.V. Neimark, Density functional theory methods for characterization of porous materials, Colloids Surf., A 437 (2013) 3–32.

[30] B. Liu, C. Li, Y. Ren, Y. Tan, H. Xi, Y. Qian, Direct synthesis of mesoporous ZSM-5 zeolite by a dual-functional surfactant approach, Chem. Eng. J. 210 (2012) 96–102.
[31] H. Huang, X. Ye, W. Huang, J. Chen, Y. Xu, M. Wu, Q. Shao, Z. Peng, G. Ou, J. Shi, X. Feng, Q. Feng, H. Huang, P. Hu, D.Y.C. Leung, Ozone-catalytic oxidation of gaseous benzene over MnO2/ZSM-5 at ambient temperature: catalytic deactivation and its suppression, Chem. Eng. J. 264 (2015) 24–31.
[32] K. Urata, S. Furukawa, T. Komatsu, Location of coke on H-ZSM-5 zeolite formed in the cracking of n-hexane, Appl. Catal., A: Gen. 475 (2014) 335–340.
[33] A. Primo, H. Garcia, Zeolites as catalysts in oil refining, Chem. Soc. Rev. 43 (2014) 7548–7561.
[34] S. Triwahyono, A.A. Jalil, R.R. Mukti, M. Musthofa, N.A.M. Razali, M.A.A. Aziz, Hydrogen spillover behavior of Zn/HZSM-5 showing catalytically active protonic acid sites in the isomerization of *n*-pentane, Appl. Catal., A: Gen. 407 (2011) 91–99.
[35] M. Sánchez-Sánchez, T. Blasco, Characterization of zeolite basicity using probe molecules by means of infrared and solid state NMR spectroscopies, Catal. Today 143 (2009) 293–301.
[36] H. Förster, H. Fuess, E. Geidel, B. Hunger, H. Jobic, C. Kirschhock, O. Klepel, K. Krause, Adsorption of pyrrole derivatives in alkali metal cation-exchanged faujasites: comparative studies by surface vibrational techniques, X-ray diffraction and temperature-programmed desorption augmented with theoretical studies, Phys. Chem. Chem. Phys. 1 (1999) 593–603.
[37] M.A.A. Aziz, A.A. Jalil, S. Triwahyono, M.W.A. Saad, $CO_2$ methanation over Ni-promoted mesostructured silica nanoparticles: influence of Ni loading and water vapor on activity and response surface methodology studies, Chem. Eng. J. 260 (2015) 757–764.
[38] J.C. Lavalley, Infrared spectrometric studies of the surface basicity of metal oxides and zeolites using adsorbed probe molecules, Catal. Today 27 (1996) 377–401.
[39] C.A. Emeis, Determination of integrated molar extinction coefficients for infrared absorption bands of pyridine adsorbed on solid acid catalysts, J. Catal. 141 (2) (1993) 347–354.
[40] R. Srivastava, M. Choi, R. Ryoo, Mesoporous materials with zeolite framework: remarkable effect of the hierarchical structure for retardation of catalyst deactivation, Chem. Commun. (2006) 4489–4491.
[41] Y. Nakasaka et al., Deactivation mechanism of MFI-type zeolites by coke formation during *n*-hexane cracking, Chem. Eng. J. (2014), http://dx.doi.org/10.1016/j.cej.2014.11.026.
[42] J. Zhang, Z. Xin, X. Meng, Y. Lv, M. Tao, Effect of $MoO_3$ on structures and properties of Ni-$SiO_2$ methanation catalysts prepared by the hydrothermal synthesis method, Ind. Eng. Chem. Res. 52 (2013) 14533–14544.
[43] M.M. Zyryanova, P.V. Snytnikov, R.V. Gulyaev, Yu.I. Amosov, A.I. Boronin, V.A. Sobyanin, Performance of Ni/$CeO_2$ catalysts for selective CO methanation in hydrogen-rich gas, Chem. Eng. J. 238 (2014) 189–197.
[44] Y.S. Cheng, M.A. Peña, K.L. Yeung, Hydrogen production from partial oxidation of methane in a membrane reactor, J. Taiwan Inst. Chem. E 40 (2009) 281–288.
[45] D.-W. Jeong, A. Jha, W.-J. Jang, W.-B. Han, H.-S. Roh, Performance of spinel ferrite catalysts integrated with mesoporous $Al_2O_3$ in the high temperature water-gas shift reaction, Chem. Eng. J. 265 (2015) 100–109.
[46] T. Miyao, S. Sakurabayashi, W. Shen, K. Higashiyama, M. Watanabe, Preparation and catalytic activity of a mesoporous silica-coated Ni-alumina-based catalyst for selective CO methanation, Catal. Commun. 58 (2015) 93–96.
[47] H.D. Setiabudi, A.A. Jalil, S. Triwahyono, N.H.N. Kamarudin, R. Jusoh, Ir/Pt-HZSM5 for *n*-pentane isomerization: effect of Si/Al ratio and reaction optimization by response surface methodology, Chem. Eng. J. 217 (2013) 300–309.
[48] H.D. Setiabudi, A.A. Jalil, S. Triwahyono, Ir/Pt-HZSM5 for *n*-pentane isomerization: effect of iridium loading on the properties and catalytic activity, J. Catal. 294 (2012) 128–135.
[49] E. Blomsma, J.A. Martens, P.A. Jacobs, Reaction mechanisms of isomerization and cracking of heptane on Pd/H-Beta zeolite, J. Catal. 155 (1995) 141–147.
[50] F. Chen, L. Ma, D.-G. Cheng, X. Zhan, Synthesis of hierarchical porous zeolite and its performance in *n*-heptane cracking, Catal. Commun. 18 (2012) 110–114.
[51] D. Liu, S. Hua, R. Lau, A. Borgna, G.L. Haller, Y. Yang, Hydroconversion of *n*-heptane over Pt/Al-MCM-41 mesoporous molecular sieves, Chem. Eng. J. 151 (2009) 308–318.
[52] M.A.A. Aziz, A.A. Jalil, S. Triwahyono, R.R. Mukti, Y.H. Taufiq-Yap, M.R. Sazegar, Highly active Ni-promoted mesostructured silica nanoparticles for $CO_2$ methanation, Appl. Catal., B: Environ. 147 (2014) 359–368.
[53] Q. Pan, J. Peng, T. Sun, S. Wang, S. Wang, Insight into the reaction route of $CO_2$ methanation: promotion effect of medium basic sites, Catal. Commun. 45 (2014) 74–78.
[54] R. Razzaq, C. Li, M. Usman, K. Suzuki, S. Zhang, A highly active and stable $Co_4N$/$\gamma$-$Al_2O_3$ catalyst for CO and $CO_2$ methanation to produce synthetic natural gas (SNG), Chem. Eng. J. 262 (2015) 1090–1098.
[55] J. Zhang, X. Zhang, W. Liu, H. Liu, J. Qiu, K. L Yeung, A new alkali-resistant Ni/$Al_2O_3$-MSU-1 coreeshell catalyst for methane steam reforming in a direct internal reforming molten carbonate fuel cell, J. Power Sources 246 (2014) 74–83.
[56] S. Kiatphuengporn, M. Chareonpanich, J. Limtrakul, Effect of unimodal and bimodal MCM-41 mesoporous silica supports on activity of Fe–Cu catalysts for $CO_2$ hydrogenation, Chem. Eng. J. 240 (2014) 527–533.